Decomposition and Description of the Nasal Cavity Form

A. M. GAMBARUTO,[1,2] D. J. TAYLOR,[2,3] and D. J. DOORLY[2]

[1]CEMAT, Department of Mathematics, Instituto Superior Técnico, Lisbon 1049-001, Portugal; [2]Department of Aeronautics, Imperial College London, South Kensington Campus, London SW7 2AZ, UK; and [3]Department of Bioengineering, Imperial College London, South Kensington Campus, London SW7 2AZ, UK

Associate Editor John H. Linehan oversaw the review of this article.

Abstract—Patient-specific studies of physiological flows rely on anatomically realistic or idealized models. Objective comparison of datasets or the relation of specific to idealized geometries has largely been performed in an *ad hoc* manner. Here, two rational procedures (based respectively on Fourier descriptors and medial axis (MA) transforms) are presented; each provides a compact representation of a complex anatomical region, specifically the nasal airways. The techniques are extended to furnish average geometries. These retain a sensible anatomical form, facilitating the identification of a specific anatomy as a set of weighted perturbations about the average. Both representations enable a rapid translation of the surface description into a virtual model for computation of airflow, enabling future work to comprehensively investigate the relation between anatomic form and flow-associated function, for the airways or for other complex biological conduits. The methodology based on MA transforms is shown to allow flexible geometric modeling, as illustrated by a local alteration in airway patency. Computational simulations of steady inspiratory flow are used to explore the relation between the flow in individual vs. averaged anatomical geometries. Results show characteristic flow measures of the averaged geometries to be within the range obtained from the original three subjects, irrespective of averaging procedure. However the effective regularization of anatomic form resulting from the shape averaging was found to significantly reduce trans-nasal pressure loss and the mean shear stress in the cavity. It is suggested that this may have implications in attempts to relate model geometries and flow patterns that are broadly representative.

Keywords—Nasal airflow, Geometry characterization and deconstruction, Geometry average, Modal analysis, Radial basis function, Fourier descriptors, Medial axis.

INTRODUCTION

Exploring the link between anatomical form and physiological function is of long-standing interest and importance, particularly for healthcare applications. A particular objective is to understand how key geometric attributes can affect normal and pathological function, which is relevant for the diagnosis and prognosis stages of clinical management. The work described here focuses on the nasal airways, which constitute a biological conduit of remarkably complex form. It is anticipated therefore that the methods and procedures of this investigation could be applied to other application areas in which the study of geometrical form within a population is of interest, and not only to those concerned with respiratory biomechanics.

This study presents rational approaches to describe the nasal airways and to provide a compact representation that can be used to formulate a modal analysis about an average geometry. The average geometries are compared to the patient-specific cases, in both morphology and computed flow field, in order to indicate the degree of similarity of inspired airflow with respect to the description of the form.

The nasal cavity provides a remarkable study of how geometric form (see Fig. 1) controls flow in order to achieve disparate physiological functions. The three principal roles of the nose are: (i) to warm and humidify inspired air efficiently, with partial recovery of both heat and humidity on expiration; (ii) to protect and defend the lower respiratory tract by filtering and trapping particles and some pathogens; (iii) to facilitate sensing of inspired air by the olfactory receptors which are concentrated in the olfactory cleft, in the superior and posterior region of the cavity.[3,27,41] The nasal cavity morphology is widely variable both inter- and intra-individually. Intra-individual variations encompass both permanent differences between the left and

Address correspondence to A. M. Gambaruto, CEMAT, Department of Mathematics, Instituto Superior Técnico, Lisbon 1049-001, Portugal. Electronic mail: agambar@math.ist.utl.pt
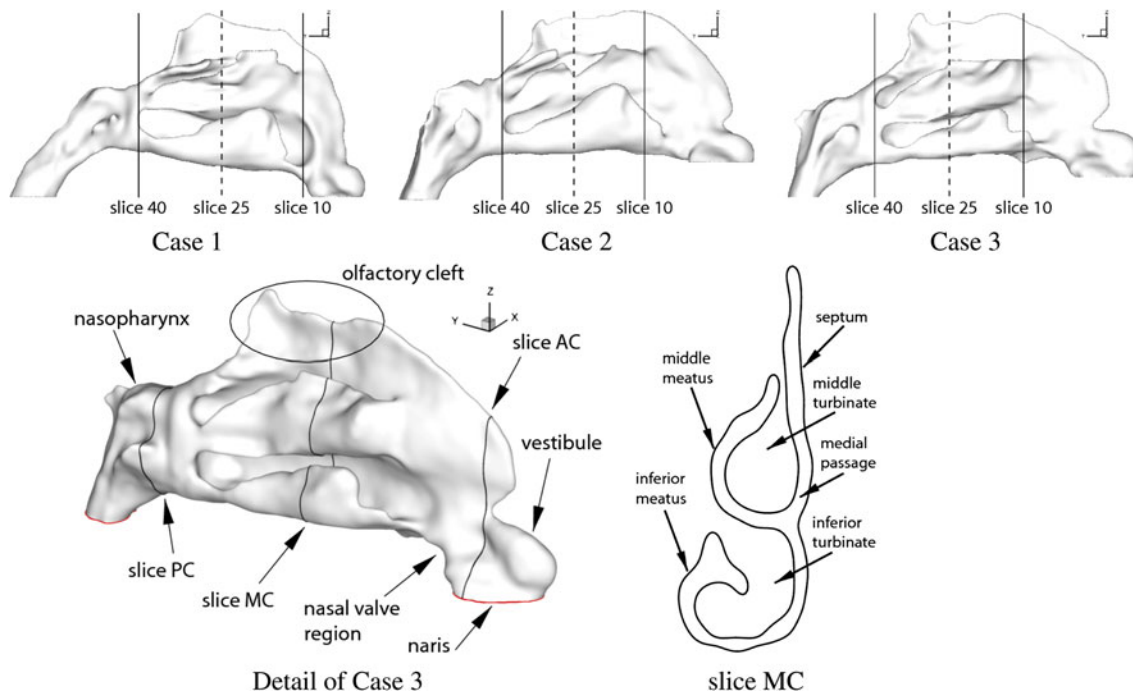
FIGURE 1. Top row: sagittal views of three subject cases with the start and end of the middle meatus in the coronal plane identified by the solid lines. Using these landmarks the airway is divided into three regions: anterior, middle and posterior cavity. The dashed line indicates the location of slice 25 in the stack, which is used as example cross-section in most figures. Bottom row: nomenclature of right nasal cavity airway (subject Case 3). The surface shown is the boundary of the airway to surrounding solid structure. The location of illustrative coronal slices taken in the anterior (AC), middle (MC) and posterior (PC) cavity regions are also shown.

right nasal passages on account of differences in structure, and temporal variations in passage calibre. Temporal variations are associated with mucosal tissue engorgement and may arise spontaneously (with the nasal cycle, or as a reaction to an allergen or infection[12]). Inter-individual variations are marked, with a wide variety of morphological forms observed.[8,24,25]

Studies of nasal airflow are motivated both by a desire to increase understanding of respiratory physiology and to provide knowledge for possible applications in surgery, drug delivery and toxicology. The nasal cavity surface is rich in blood vessels, including arterioles and capillaries.[3,27] It thus provides an inhalation-based portal for drug delivery, with rapid absorption by the mucosa into the circulatory system obviating the need for invasive administration, as discussed in Illum,[20] Kleven et al.,[23] and Schroeter et al.[32]

Previous studies have successfully applied computational tools to study the complex form of the human nasal airways. A Fourier descriptor based method was shown to provide a compact approach to describe the nasal passage, and to generate reduced models using signal filtering.[18] In a complementary approach, a modal analysis technique applied to a reduced medial axes representation of the inferior meatus demonstrated a means to deconstruct the complex anatomy into its constituent geometric features.[9] More recently

a standardized nasal cavity geometry was proposed by Liu et al.[25] that was formulated by averaging binary images of cross-sections of previously scaled and aligned geometries. However, this approach did not yield a compact representation of the geometry studied but simply a means to obtain an average.

Other computational tools for shape description have been employed for specific medical applications. Parametric models have been used to study arterial bifurcations[43] and the principal arterial vessels in the cerebral vasculature[28] for correlation studies with cerebral aneurysm formation. Other work has used Zernike moments to correlate geometry to the rupture of cerebral aneurysms.[26] Methods for three-dimensional harmonic maps of brain volume have been outlined in Wang et al.,[39] while a preliminary study on using surface harmonic mapping of the nasal cavity has been presented in Gambaruto[14]; both methods provide a means to construct a common frame of reference upon which a comparative analysis (of computational or experimental results) can be performed as well as providing distortion-energy maps that can be used to describe the geometry. Parametric surface description using spherical harmonics as basis functions have also been successfully applied to describe the hippocampus,[34] allowing a hierarchical approach to shape representation. Closely related to

the medial axis (MA) transform discussed in this work, a modal analysis of medial-atoms has been used in the study of kidney surface models.[13] The above methods are not readily generalized for use with any complex geometry surface, and most do not provide a means to formulate a modal analysis about an average, nor do they allow for a reversible compact description.

There have been several studies to investigate how the interior and exterior morphology of the nose affects the flow within the human nasal passages.[1,8,10,31] Some relations between geometric attributes and the associated flow field have been identified such as: the role of the nasal valve in directing the flow; the influence of the turbinates as protrusions that interrupt and partition flow, enhancing transport and exchange processes; and the preponderance of air that is transported to the olfactory cleft originating from in front of the nose. The present work sets out to demonstrate how nasal geometry and flow may be systematically investigated with the advantage of a rational basis capable of describing specific inter- or intra-subject morphological differences. However, it is recognized that the inflow boundary conditions are also important in determining nasal airflow. As reported in Doorly *et al.*,[10] and Taylor *et al.*,[36] sensitivity of the resulting flow field was observed for varying inflow boundary conditions (both for steady and unsteady flows). Whilst the steady assumption for nasal airflow is not fully correct, the unsteady characteristics of nasal airflow are highly variable, inter- and intra-subjectively.[29] Nevertheless, in order to outline a new, rational approach to characterise variations in nasal form and consequences for the flow, the steady flow assumption, restricted to the case of quiet restful breathing may be considered sufficient.

In the following sections, the methods used to generate a compact and hierarchical description of the nasal passageways of three healthy subjects are outlined. The proposed approach is demonstrated using anatomically realistic 3D virtual models, that are obtained by reconstructing the nasal geometry from a stack of Computed Tomography (CT) images obtained

in vivo, discussed briefly in "Subject Datasets" section. Subsequently, in "Methods for Surface Decomposition and Compact Description" section, reversible decompositions are described, which use two alternative shape descriptors to provide compact representations of the anatomical surfaces and the formulation of an average geometry. Computational simulations of steady inspiratory airflow are provided and the resultant flow fields are compared for all the subjects and average geometries in "Results" section. The Discussion is presented in "Discussion" section and finally some scope for further work and conclusions are provided in "Conclusions" section.

SUBJECT DATASETS

For the three subjects considered, the nasal airway geometry data is given in the form of a stack of *in vivo* medical images obtained using CT acquired in the axial plane. The resulting image parameters are: 512×512 pixels, 1.3 mm slice thickness, 0.7 mm slice spacing, 0.39×0.39 mm pixel size. For each patient between 80 and 85 images were acquired to cover the nasal cavity (see Table 1 for the individual heights). The CT image datasets used were obtained with permission by retrospective examination of clinical records from the ENT surgical department at St. Mary's Hospital, Paddington, London. A small proportion of clinically referred subjects displayed airway anatomies subsequently determined to be normal by a consultant ENT surgeon. The subjects provide three test cases for this research: Case 1—female, 47-years-old; Case 2—male, 31-years-old; and Case 3—female, 53-years-old.

Whilst insufficient for a comprehensive investigation of the relation between anatomic form and flow, three geometries are sufficient as a means to explain possible techniques to perform such study, which is the purpose of the present paper. Characteristic features such as nasal valve area and direction, cavity volume and turbinate morphology are very different across the three subjects (see Table 1), for example subject 2 is

TABLE 1. Geometric properties of the cases studied.

	Case 1	Case 2	Case 3	FD average	MA average	Direct average
Surface area (cm^2)	107.08	108.65	106.26	97.86	98.34	107.33
Volume (cm^2)	14.15	22.36	13.83	16.52	16.58	16.78
Length (cm)	10.63	10.95	10.53	10.61	10.63	10.70
Height (cm)	5.44	5.85	5.48	5.15	5.22	5.59
Width (cm)	1.80	1.89	1.58	1.52	1.57	1.76
∠(Nasal valve) (naris) (°)	25	35	45	35	35	35
Area of nasal valve (cm^2)	0.93	0.85	0.45	0.72	0.68	0.74

The direct average of the subject cases closely matches the average geometries. See "Average Geometry" section for discussion.

representative of a large nasal valve and highly decongested state (with a low surface area to volume ratio) and subject 3 illustrative of a more restricted nasal valve and higher surface area to volume ratio. The three geometries are shown in Fig. 1 together with an explanation of the pertinent anatomical structures.

Initial segmentation of the medical images, to identify the boundary between the airway and the surrounding tissue, was based on a constant value of the greyscale. A manual refinement of the segmentation was required to exclude secondary conduits such as those to the sinuses, as well as to identify under-resolved structures.[9,18] This was performed by an ENT surgeon familiar with the complex anatomy, using commercial software (Amira, Mercury Computer Systems, Inc., UK), and yielded step-like surfaces for each nasal cavity surface segmented.

The segmented surfaces have an inherent imaging uncertainty of one pixel, though the machine resolution may be coarser due to focusing accuracy and artefacts. The methods presented here are hence constrained to operate within this error bound. Due to the pixelated nature and the presence of noise in the medical images, the resulting surfaces are unrealistically rough and surface smoothing is necessary. Care must be taken in the smoothing procedure to ensure fidelity with the medical images. Smoothing is performed by iteratively moving the nodes of the constructed surface mesh using the local connectivity information. The surface smoothing adopted is based on the bi-Laplacian method with anisotropic smoothing discussed in detail in Gambaruto et al.[18]

Registration of all reconstructed virtual models was performed to optimally align the geometries to a common orientation, using rigid body transformations. This allows for the measurement of differences in the geometries and the resulting flow solution. The registration method used is based on the iterative closest point (ICP) method,[4,15,30] For simplicity, both visually and computationally, the analysis performed is limited to the right nasal cavity in this work.

METHODS FOR SURFACE DECOMPOSITION AND COMPACT DESCRIPTION

A compact representation that allows characterization and inter-subject comparison of morphologies is now described. The approach proposed is based on two steps: first, section the geometry surface to obtain a stack of closed curves; second, represent each of these cross-sections by either Fourier descriptors (FDs) or medial axes. The techniques used are reversible such that the surface can be reconstructed from the compact representation without a significant loss of information

(to a desired error bound), though the number of slices used should be sufficient to provide a faithful description of the surface.

To reconstruct the original surface from the stack of contours, an implicit function formulation with cubic radial basis function (RBF) interpolation is used. This approach is robust, flexible and provides an accurate surface representation if given sufficient information from which to interpolate.[18]

The cross-sections are described using either FDs or medial axes. The FDs method first requires that each closed curve be represented as a periodic signal, typically using curvature or position (with respect to a fixed orthogonal coordinate system) as a function of curve length, and secondly a Fourier series expansion of this signal is performed. The medial axes approach identifies the supporting frame of the closed curves, embedding the local calibre information. This allows the geometry to be manipulated directly using the underlying compact description. Both techniques introduce the formulation of a modal decomposition of the form $\Psi = \sum_{i=1}^{N} \alpha_i \psi_i$, where the modes ψ_i have decreasing energy α_i for increasing i. This provides a convenient form to perform filtering or data compression. This representation can describe a subject data set as a sum of weighted perturbations about an average (standardized) nasal cavity geometry.

Reversibility of each decomposition step signifies that the compact description can accurately reproduce the surface description. The level of accuracy depends on: the number of cross-sections taken and the interpolation scheme used, the number of Fourier modes (if filtering is performed) or the number of medial axes considered (if pruning is performed).

In this work 50 coronal slices are used, as shown in Fig. 2, specifically 10 equally spaced slices were taken in the anterior and posterior segments of the cavity while 30 equally spaced slices were taken in the middle cavity section. The number of slices used was determined based on the local complexity of the nasal anatomy but has not been optimized. The choice represents a balance between minimising computational cost while retaining the desired level of geometric complexity. The three regions were delineated using the criterion that the middle cavity section should fully contain the middle meatus. Using 150 uniformly spaced cross-sections in the coronal plane together with the MA decomposition, the locations of the start and end of the middle meatus formation were identified, as shown in Fig. 1.

This selection of slice locations ensures correspondence, and hence meaningful comparison, of cross-sections between the different subject datasets by using the middle meatus landmark. Other landmark features as well as non-parallel slice orientations could be

Decomposition stages

Step 1. Stack representation

Step 2. Calibre coding

Step 3. Classification coding
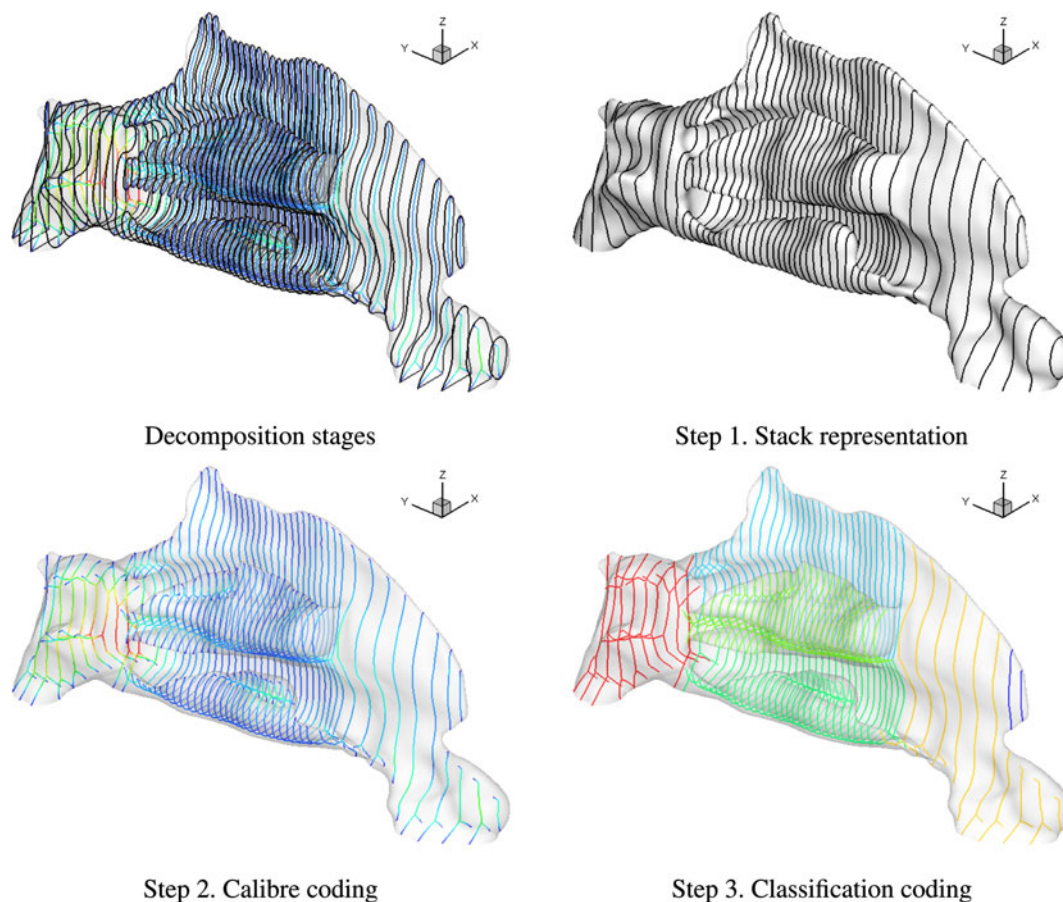
FIGURE 2. Case 3 decomposition into a stack of cross-sections that can be interpolated back to a surface representation using the implicit function approach. The stack of cross-sections can be further characterized by supporting medial axes that encode information including the local calibre and the structure classification.

introduced to refine the study. This correspondence of the equally spaced slices implicitly assumes appropriate linear scaling perpendicular to the plane of the slices, based on the landmarks chosen, hence taking into account naturally the regional size variations present among subjects.

Such considerations have many advantages: firstly, the amount of data to be processed at any time is less than considering the entire geometry; secondly, the descriptors of each cross-section are independent and can be analyzed, compared and processed separately; thirdly, different regions of the topology may be studied individually; finally, correspondence for direct inter-subject comparison is maintained.

The process of obtaining the surface from the slices *via* an RBF interpolation is discussed in "Implicit Function Interpolation" section. This is followed by a detailed description of the two methods adopted to describe the cross-sectional contours: a MA decomposition in "Medial Axes" section and the FD decomposition in "Fourier Descriptor" section. Formulation of the average geometries is detailed in "Creating an Average Geometry" section and the parameters for CFD simulations are presented in "Parameters for Flow Simulation" section

Implicit Function Interpolation

An implicit function formulation was used to reconstruct the right nasal cavity from the stack of 50 closed curves, providing the reversibility of the sectioning procedure.[18] The procedure for interpolating a surface through the contour stack is described in greater detail in Gambaruto *et al.*,[17] Giordana *et al.*,[19] and Carr *et al.*[7] Details of the implicit function method are presented in the Appendix.

The difference between the surface definitions and those obtained by slicing the geometry and reconstructing it as a test, are within $\frac{1}{2}$ pixel on average, with standard deviation $\frac{1}{5}$ and 2.5 pixel maximum difference (1 pixel = 0.39 mm). This shows that for the cases studied, the 50 slices taken are sufficient to capture the topology in detail and to reconstruct the surface within an error of the same order of magnitude as the imaging

uncertainty. The large maximum surface deviation occurs in isolated regions where the slices do not contain a feature; however this is seen in the nasopharynx for small regions (localized protrusions). It is of little relevance to the current work for inspiratory flow, as this zone is downstream of the cavity and is a region of increased patency. Increasing the number of slices reduces this error.

Medial Axes

The MA of a two-dimensional closed shape was introduced in Blum[6] as a means of extracting and describing shape and has since been used largely in the field of image processing, machine vision and 3D model description and animation.[2,35,40] The medial axes of an object can be considered to be: the location where concentric fronts expanding from the object border meet[6]; or the connected centers of the locally inscribed discs of maximum diameter, that touch the edge of the object in two or more locations.[40] Medial axis extraction for a sample cross-section is shown in Fig. 3. Details of the MA method developed here are presented in the Appendix.

The classification of the different MA branches is unambiguous and based upon the slice location (i.e., if it lies in the anterior, middle or posterior region of the nasal cavity). Main branches are identified; from these secondary branches may grow; from these tertiary branches and so on. Each branch is assigned a number that uniquely identifies its location and properties, as shown in Fig. 4. Combined with the inter-subject correspondence of the slices this enables direct comparison of individual medial axes between subjects.

The stack of 2D closed contours can hence be rendered into a stack of smooth medial axes, which encode the local calibre variation along each branch. The process can be reversed and closed contours can once again be reconstructed, which can be used to obtain the original geometric surface using the implicit function formulation. These steps allow the geometry to be described compactly and unambiguously by the stack of MA branches (i.e., the supporting frame to the geometry) to a desired error bound. Figure 2 shows the various decomposition stages using MA branches for subject Case 3.

It is important to note that the number of branches is not always the same in the different cases, however due to this classification each branch has a unique identity and features can be distinguished and considered individually. Each branch is considered separately, independent of other branch types and hence the rest of the medial axes stack.

A continuous representation in the form of a medial-axis sheet can be constructed as shown in Fig. 5, such that analysis of the supporting structure can be performed along the sheets and not only in the planes of the cross-sections. The medial sheet definition also allows for the surface and volume to be sectioned into different structures and regions. The medial sheet properties provide information about the object that they support and examples are provided in Table 2 for the cases studied.

Altering the medial axes (and sheets) has direct and intuitive consequences for the geometric boundary definition they represent. This provides a useful means to modify the boundary to, for instance, alter the passage patency (to mimic occlusions or the nasal cycle), or to perform virtual surgery on the original anatomy. Such modification is illustrated in Fig. 6 where complete and partial branch occlusion was performed. This process could equally be applied to

Slice 25   Medial axis   Inverse medial axis   Pruning   Classification
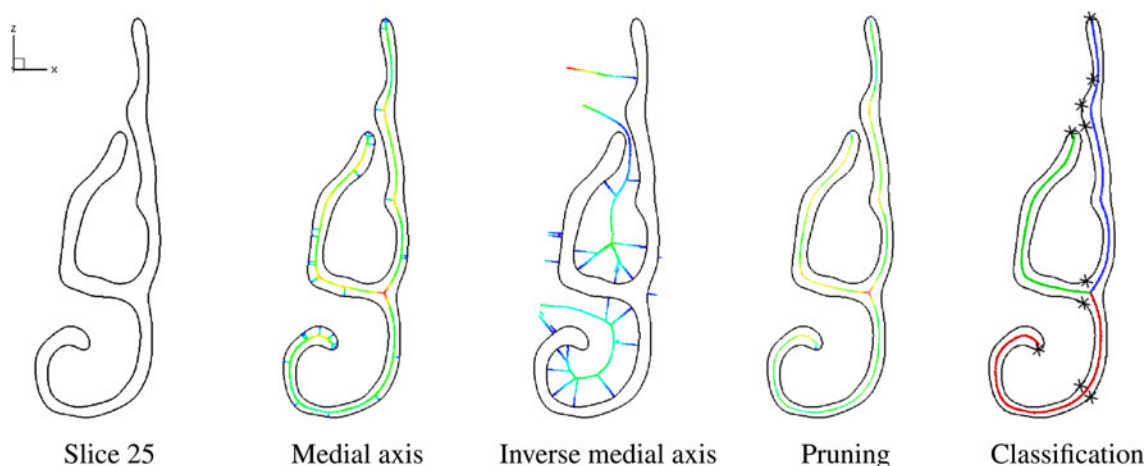
FIGURE 3. **Case 3 decomposition of a slice into the MA of the airway and surrounding tissue, here coloured by the local distance to the curve. Automatic pruning removes secondary structures. Classification of the MA branches is also possible and the perimeter can also be partitioned.**
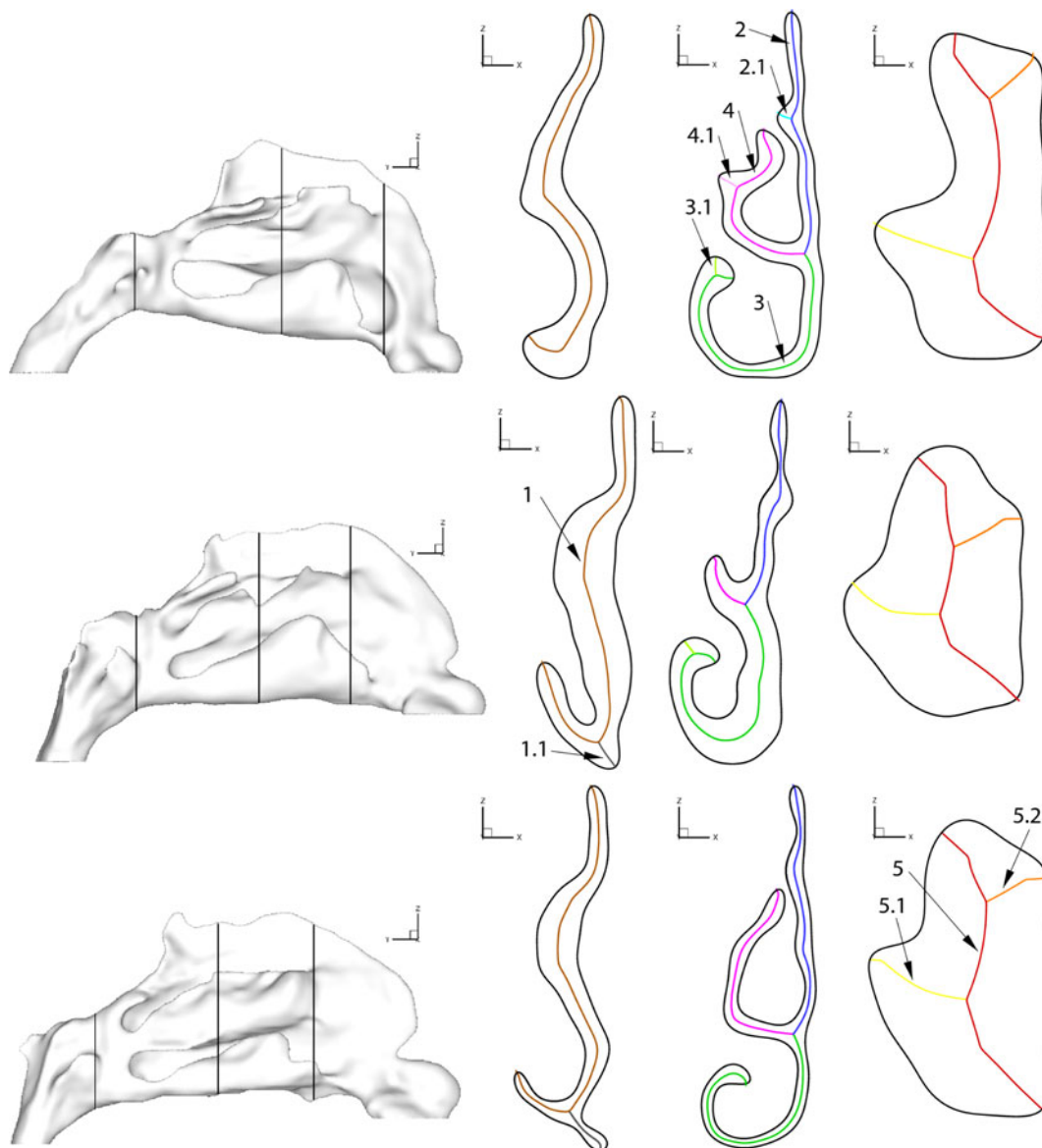
FIGURE 4. Three example slices are taken from case 1, 2 and 3 (from top to bottom) that are located in the anterior, middle and posterior sections to the nasal passage (from left to right). For each of the cross-sections the branches, coloured differently here, are assigned a number associated to their location and parent branches: brown = 1, grey = 1.1, green = 2, light green = 2.1, blue = 3, light blue = 3.1, purple = 4, light purple = 4.1, red = 5, yellow = 5.1, orange = 5.2. The number is formed such that main branches have different unit values and sub-branches have indices an order of magnitude progressively smaller. Note that in these examples only one lower branch is encountered but branches such as 4.1.1 may exist for some cross-sections.
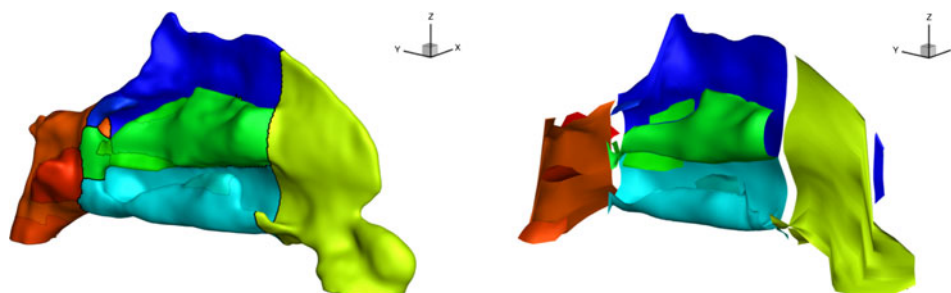
FIGURE 5. Automatic classification of the geometry surface and volume (left) and the medial sheet as the supporting structure (right), with the overhang region above the nasal valve identified separately.

TABLE 2. Medial sheet areas (cm^3) of the main medial axis branches, as shown in Fig. 5.

|	Case 1	Case 2	Case 3	MA average
Anterior section	6.2	11.7	10.8	9.3
Upper septum	10.5	9.7	10.9	10.2
Lower meatus and septum	16.5	11.3	12.0	13.2
Middle meatus	8.2	5.0	7.4	6.5
Posterior section	6.9	8.1	6.4	7.0

the inverse medial axes (shown in Fig. 3). This demonstrates the power of the MA representation as a tool in geometry description and manipulation.

Fourier Descriptor

The approach of applying FDs to characterise the nasal cavity has been introduced in Gambaruto et al.[18] Each closed contour obtained from the slices of the geometry surface is first converted to a signal which is then expanded as a Fourier series. The coefficients in
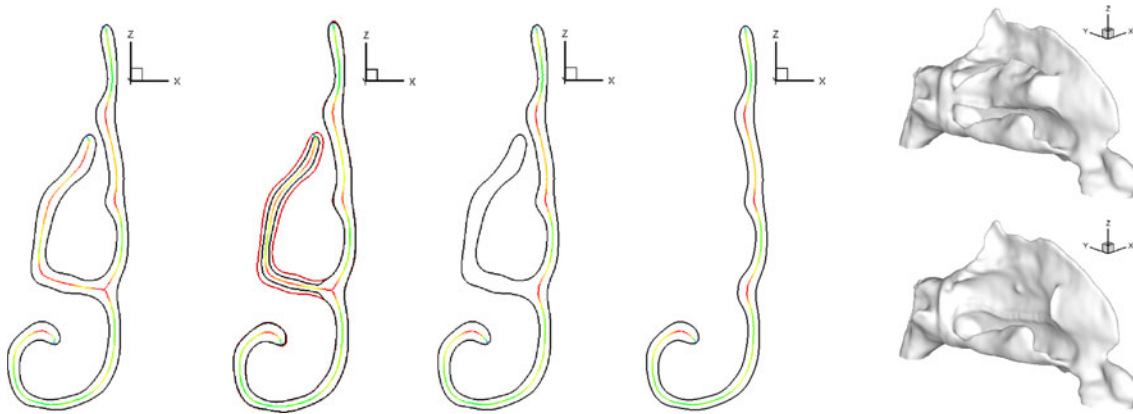
FIGURE 6. Manipulation of the MA allows for selective congestion (other forms are also possible) or complete removal of features. This is performed on the cross-sections and the reconstructed surface geometry mirrors these changes.

Case 1 Case 2 Case 3

FD average MA average FD average - MA average
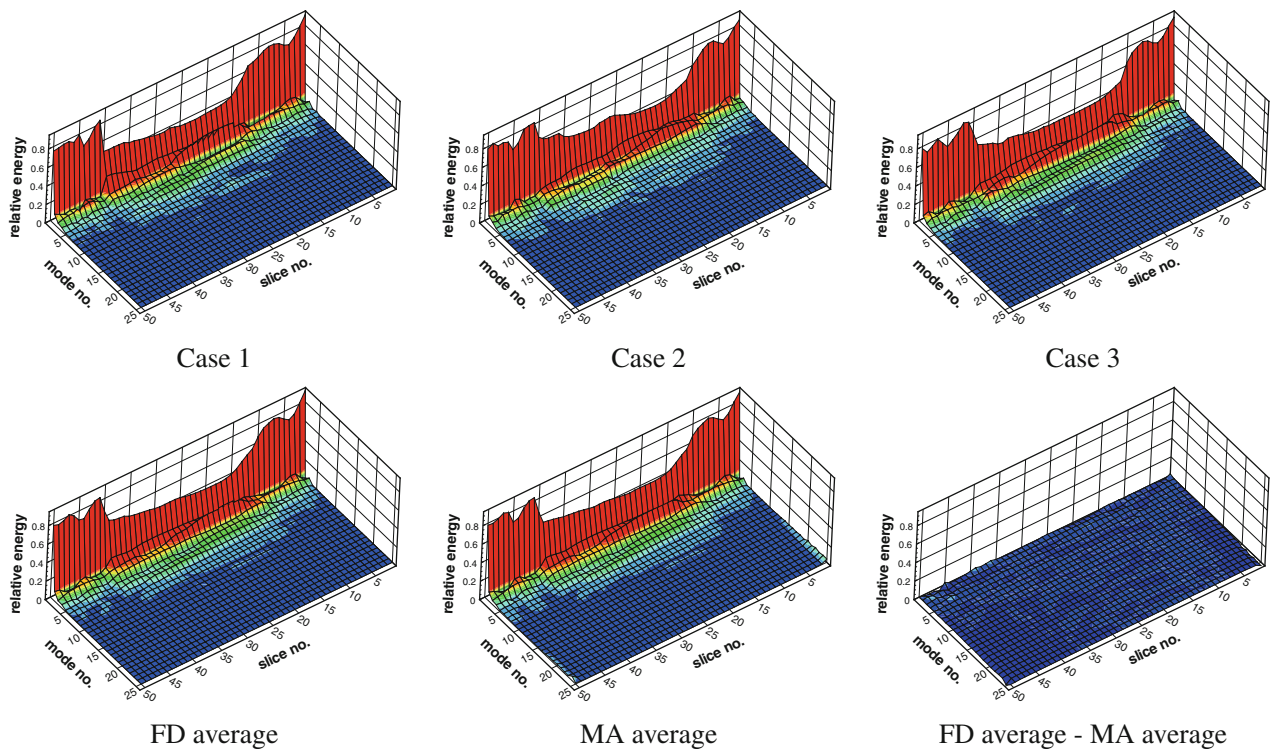
FIGURE 7. Energy maps of the FDs for the stack of contours for the geometries studied. It is evident that a few modes are the energy carrying ones. Furthermore the FD and MA average geometries have signals that are very similar to each other as seen by subtracting one from the other.

the Fourier expansion are termed the Fourier descriptors. Shape characterization can be performed by analysing the energies in the modes, while filtering the signal to retain the dominant modes is useful for data compression. Details of the FD method are presented in the Appendix.

In Fig. 7 the amplitudes of the modes are shown for the three subject datasets. It is evident that the dominant modes are those with lowest frequency, with modal energy quickly decreasing for higher modes. There is a slight increase in the energy carried by higher frequency modes within the mid-cavity region due to the increased complexity of the constituent cross-sections. These results are consistent with those reported in Gambaruto *et al.*,[18] where the signal used was based on a curvature variation, as opposed to the change in location coordinates used here. A low-pass filter was used to perform a simple truncation of the series to keep the first 50 modes. This has been used for simplicity in this study to keep only the dominant modes (preserving ~99.9% of the original signal energy).

In Gambaruto *et al.*[18] the flow field in both the filtered and original geometry of Case 3 have been compared. It was found that the flow field remained largely unchanged when filtering was applied to remove all but the underlying 15 dominant modes (with ~95% energy) in the Fourier series. Truncating the Fourier series at 50 modes is therefore justified in this study as a more accurate description of the geometry is ensured. This is especially relevant to account for the frequency mismatch occurring in the averaging procedure, as discussed in the following section. This choice in the number of modes has not been optimized, however it should be noted that the use of a large set of modes does not impact significantly on the computational cost.

Creating an Average Geometry

It can often be useful to perform analysis on a population average as a possible means to obtain a broad outline of the problem to be studied. Moreover the possibility of performing a modal analysis, such that each individual case is a set of perturbations from the average, is an appealing and powerful tool. In this section details of how to obtain an average nasal cavity geometry and perform a modal analysis using the methods outlined above are presented. Firstly the medial axes method for formulating an average is detailed, followed by the FD approach.

As discussed in "Medial Axes" section, the medial branches for each cross-section can be extracted and classified. To construct an average, each branch is first discretized into an equal number of uniformly spaced points (medial atoms). These individual points can be considered to be directly corresponding to those in the other subject cases: the average position and local calibre is simply the average of the these properties. If an individual case does not have a specific sub-branch then a ghost branch (a single point with zero calibre) is introduced, located at an average distance along the parent branch (calculated from the remaining cases). In this way no bias is introduced while still providing information to the modal analysis indicating no branch present. It is worth mentioning that a modal analysis such as proper orthogonal decomposition (POD), could be performed directly on the medial atoms, as proposed in Kappagantu and Feeny[21] for their study on vibrating cantilever beams. This would allow for an optimal (linear) series expansion specific to the geometry set studied, hence the modes of perturbation about the mean will be more informative than the Fourier modes. Other representations of the medial branches may also be used, such as curvature variation[9,14] or by using splines and other means to represent a curve, permitting flexibility and development of the method.

Obtaining the average geometry using the FD approach requires care since, in the same way that the medial axes are divided into corresponding branches, the correspondence of various segments of the cross-sectional curve is required for a meaningful comparison. These segments are identified in this work with the aid of the medial axes since these have been calculated, and as shown in Fig. 3 the tips and roots of the MA branches yield markers. However other criteria can be adopted and different markers identified; one such example are the peaks in the signal of curvature vs. perimeter length.[18] The remaining locations at the bottom of the septum are given by choosing the furthest most bottom-right location. In regions where a feature is not present, a similar approach is used to that of the missing MA branch, hence the marker locations for this missing feature are still required and are found by use of the average ratio of the two neighbouring segments of the remaining cases.

The regions delineated by these markers are considered individual features and are parametrized using an equal number of uniformly spaced points. To calculate an average geometry from the Fourier descriptors, these segments are stretched to have uniform lengths of segments and hence regional correspondence of the curve. Once the Fourier transform has been performed, the coefficients of the series can be analyzed and averaged directly. However, equivalent stretching back to an appropriate length is required when the curves are reconstructed. This can create a mismatch of frequencies as can be seen in Fig. 8 in the region of the superior meatus (when using less than 10 dominant modes to reconstruct the curve). This mismatch is created because an equal number of points was used for all the segments of the curve. More appropriate

5 modes   10 modes   20 modes
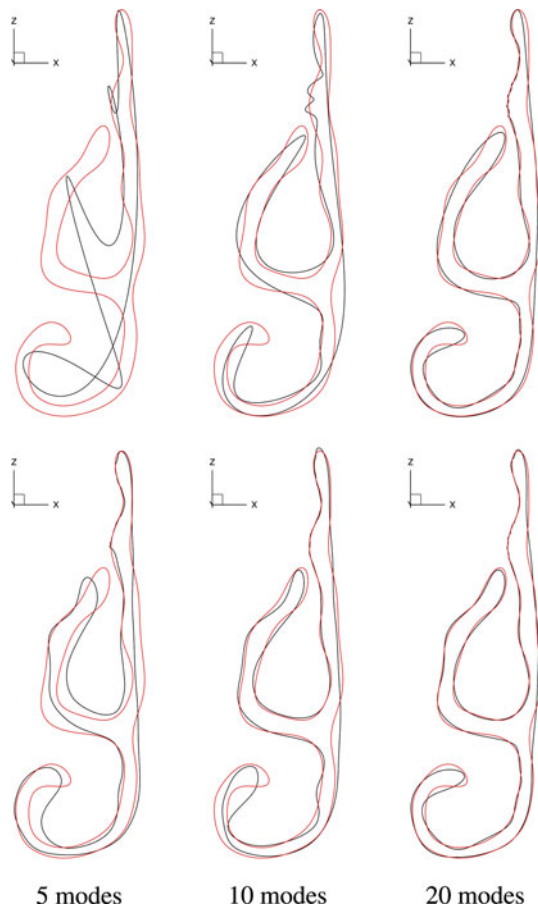
FIGURE 8. Reconstruction of slice 25 for Case 3 (black) using increasing number of FDs (given at the bottom). Top three images: increasing number of dominant Fourier modes of Case 3 only; bottom three images: increasing number of dominant Fourier perturbations from the average cross-section signal. The cross-section is divided and normalized based on the markers shown in Fig. 3. Oscillations at the superior meatus (top row for 5 and 10 modes) are caused by frequency mismatching, and for a reduced set of modes the curve is better approximated using the perturbation on top of the average signal (bottom row).

discretization taking into account the local perimeter length could be used to eliminate this mismatch. To formulate an average geometry a larger number of Fourier modes were retained (99.9% of the energy) in order to retain the frequencies that compensate for the mismatch, hence the effect is not significant. Furthermore if performing signal filtering on a single geometry this correspondence of features is not required and no spurious frequencies are therefore introduced.[18]

Parameters for Flow Simulation

A uniform velocity profile (≈ 1.0 m s^{-1}) was applied at the inflow boundary, representing a volume flux of 100 mL s^{-1} ($Re \approx 900$ based on the hydraulic diameter of the nasal valve) equivalent to quiet restful breathing. This is low enough for the flow to be laminar, as verified

for subject Case 3 by *in vitro* experiment using an anatomically accurate replica.[9] Moderately higher flow rates lead to unsteady laminar flow field.[9] The outflow boundary condition was set as constant pressure.

The volume mesh consists of four prismatic elements across the boundary layer and an unstructured tetrahedral mesh core, for a total of ~8 M cells. The height of the prismatic element nearest to the wall is 0.035 mm. A mesh convergence analysis was carried out considering subject Case 3, and the mean local error in WSS between a 3.5 and 15 million cells was found to be 8%. The computational setup used is further detailed in Gambaruto *et al.*[18] and Doorly *et al.*[9]

The numerical schemes are based on finite volume solutions of the steady incompressible, Newtonian, Navier–Stokes equations using Fluent v. 6.3.26 (Fluent, ANSYS, Inc., PA, USA). The pressure was solved using a second order accurate scheme, the pressure–velocity is coupled using the SIMPLE method and the momentum is approximated using a third order upwind scheme. The segregated approach to solving the algebraic equations of continuity and momentum is used.

RESULTS

Average Geometry

Qualitative comparison of the average geometries and cross-sections of the entire data set are presented in Fig. 9. The most striking effect of performing the average is to simplify the geometry, hence a straighter septum and the meatuses have a relatively constant radius of curvature. The cross-sectional properties for all the geometries are shown in Fig. 10 while the energy maps of the Fourier modes are shown in Fig. 7. From these it can be seen that there is little difference between the average geometries obtained using the different approaches. The large scale features of the geometries are compared in Table 1 where many measures obtained from the average geometries are reflected in the direct average calculated, indicating meaningful and representative geometric properties are preserved in the averaging processes. The averages do not exactly match the direct average for the following reasons: the reduction in the surface area in the MA approach is caused by the pruning; the reduction in surface area in the FD approach is caused by volume conservation over surface area; differences in the height and width are caused by the simplified shape of the lower meatus and septum as opposed to shorter conduits. Use of a larger population data set is expected to provide similar results qualitatively.

Small perturbations about the average generate the distinct subject cases, as can be seen in Fig. 8 for a sample slice. This can be considered to be a modal
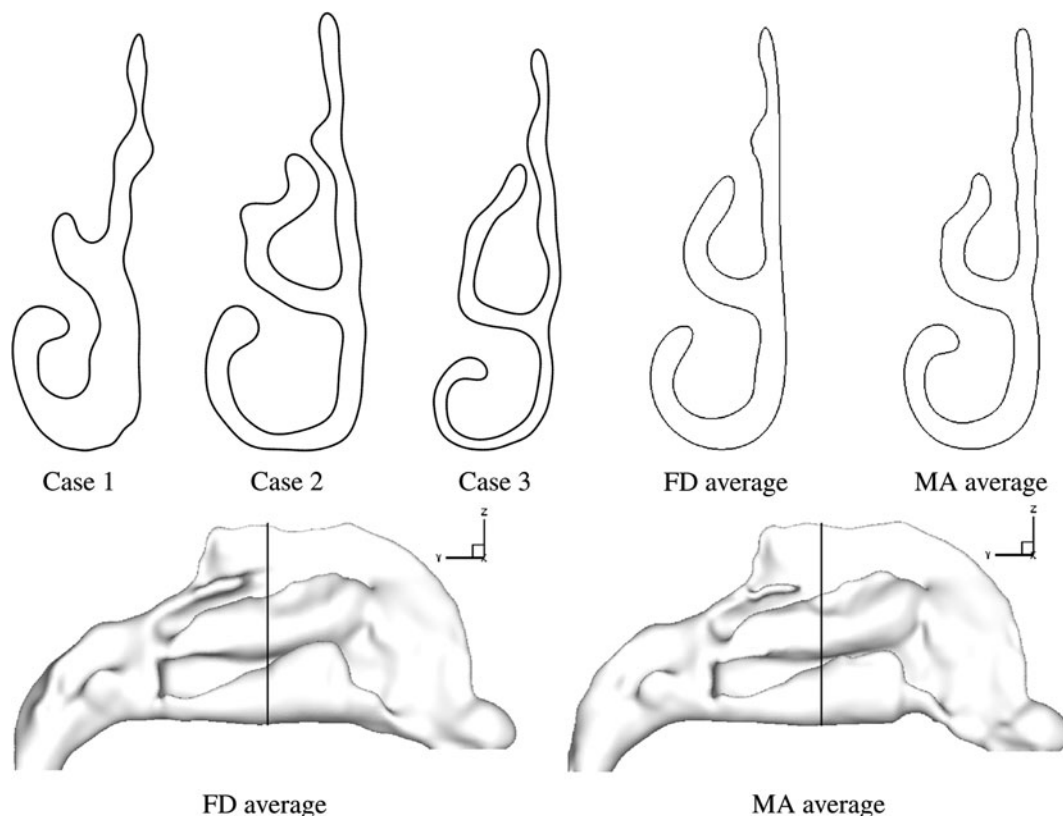
FIGURE 9. Top row: corresponding slices for the three subject cases and the FD and MA averages. Bottom row: FD and MA average geometries with the cross-section location indicated (slice 25, see Fig. 1). Note that the MA average has a higher floor just after the nasal valve and prior to the inferior meatus regions due to the pruning procedure. The overhang region above the nasal valve has effectively collapsed for these average geometries but may be present in a larger dataset.

analysis, and it is evident that the number of modes required to reconstruct the cross-section accurately is less if using perturbations about the average geometry as opposed to using single subject FDs. Furthermore the spurious frequencies are noticeably attenuated by using the perturbations about a mean geometry. This leads to the possibility of classifying a subject as a weighted set of perturbations about the mean, allowing for a quantitative analysis and population study, possibly recognizing certain geometric traits in association to healthcare issues and respiratory function. Note that the perturbations used in Fig. 8 are based on the Fourier modes and are not optimal (though they are orthogonal); this could be achieved for example, by use of the POD method.

Flow Simulation

The average geometries have been shown to be consistent representations of the individual cases through the compact representations. It remains to analyze the subject and average geometries with respect to the resulting flow solution in order to relate form to the function. This is especially important since

the average geometries are artificially generated and may not exhibit a physiologically meaningful flow field. Some measures are presented in Table 3 to provide quantitative comparisons of flow. Though the values obtained are typically within the range of values from the individual replica geometries, some differences are present. These differences can be attributed to the simplified geometric form of the average cavity, with the straighter septum, more circular meatuses and reduced surface area. For example the pressure drop across the cavity is significantly less than for the direct average.

Illustrative particle tracks, shown in Fig. 11, provide a qualitative flow description, and highlight similarities between the individual and average cases. The largest difference seen is for Case 1, where no separation region is formed above the nasal valve, while the two average geometries compare well. The wall shear stress patterns and magnitudes together with the surface shear lines, shown in Fig. 12, indicate a strong similarity between the average geometries and comparable trends with the individual cases. From Table 3 the average wall shear stress in the middle cavity section indicates that regional values of the average
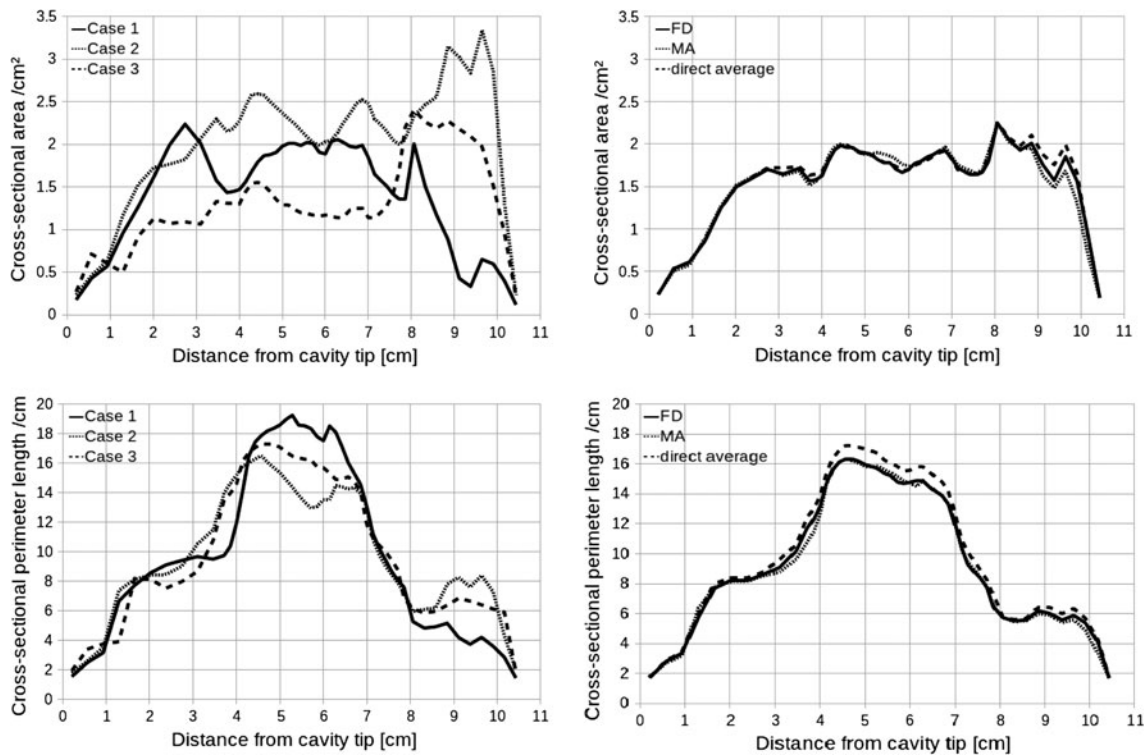
FIGURE 10. Corresponding slice properties for the three subject cases, the direct average of these, the FD and the MA averages. Top row: cross-sectional area; bottom row: cross-sectional perimeter length.

TABLE 3. Some results from the CFD of the three cases and the average geometries.

	Case 1	Case 2	Case 3	FD average	MA average	Direct average
Inflow velocity (m/s)	0.83	0.63	1.01	0.88	0.97	0.83
Pressure drop (Pa)	15.8	2.4	9.8	4.4	4.9	9.3
Mean residence time (s)	0.14	0.20	0.13	0.16	0.17	0.16
(Mean residence time)/(volume) (s/dm^3)	9.9	8.9	9.4	9.7	10.3	9.4
Mixing at slice MC (%)	2.8	11.3	10.3	6.1	9.9	8.1
Mixing at slice PC (%)	14.6	22.0	30.1	9.2	13.7	22.2
Average WSS in MC section (Pa $\times$ 10^{-2})	3.44	1.76	5.52	2.51	2.50	3.57

The mean residence time is given as the mean time for a particle to travel from naris inflow to the nasopharynx outflow. The pressure drop is calculated across the whole geometry also. It is evident that the average geometries exhibit reduced pressure drops compared to the direct average of the cases; due to the simplified form of the average and not alteration in the nasal valve that are well preserved (as shown in Table 1). The mixing is given as % of the maximum achievable mixing.[16] The average wall shear stress is calculated for the middle cavity region (see Fig. 1).

geometries are representative of the subjects. Nonetheless it is evident that geometric changes cannot be related locally to the fluid mechanics, as the effects are non-linear and have an upstream and downstream influence.

Analysing particle trajectories provides a sensitive measure of the differences between flow fields, as cumulative processes will magnify variations. An entropic measure of mixing, discussed in greater depth in Gambaruto *et al.*[16] and references therein, is used to quantify these differences. In this work this measure is obtained by seeding approximately 40,000 equi-spaced passive particles, with an associated species attribute based on their position at the naris inlet that is given by the distance from the wall. Cross-sections of the particle trajectories are obtained, as shown in Fig. 13, and the mixing is calculated considering the species of the neighbouring particle trajectories. In Table 3 the mixing at slices MC and PC (see Fig. 1) are presented. The mixing at section MC for the average geometries is representative of the average of the distinct cases, while at section PC the average geometries provide a lower value. The reason for this is likely the simplified shape of the average geometry, which affects the presence of
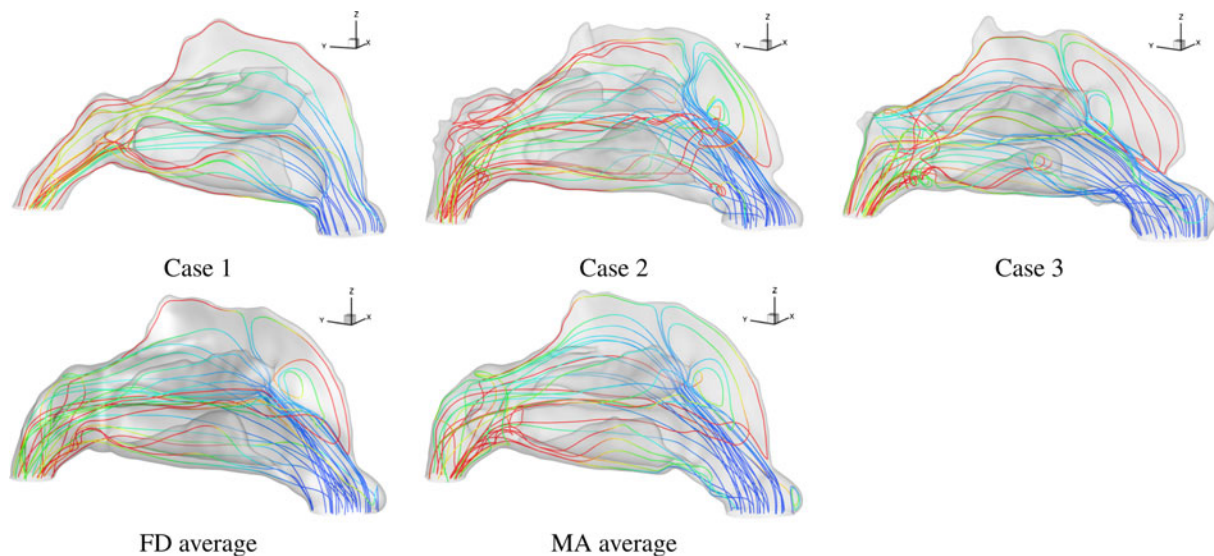
FIGURE 11. Illustrative particle tracks colour-coded by cumulative time from release at inlet section.
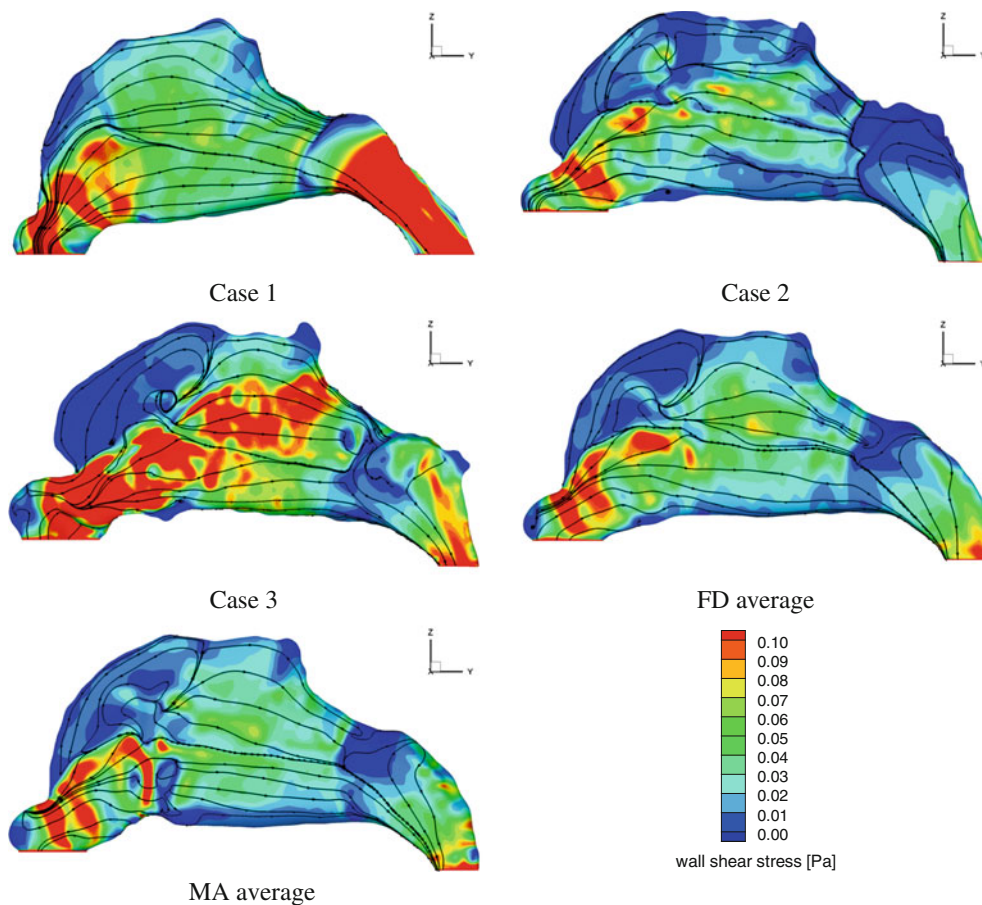

FIGURE 12. Views in the sagittal plane (of the septal wall) of the wall shear stress magnitude (Pa). Black lines indicate the surface shear lines.

secondary flows. Another measure relying on time integration along pathlines is the evacuation times; distributions are shown in Fig. 14. The average geometries indicate good agreement with the trends of the individual datasets, with the peaks forming at the same time. The average geometry constructed by the
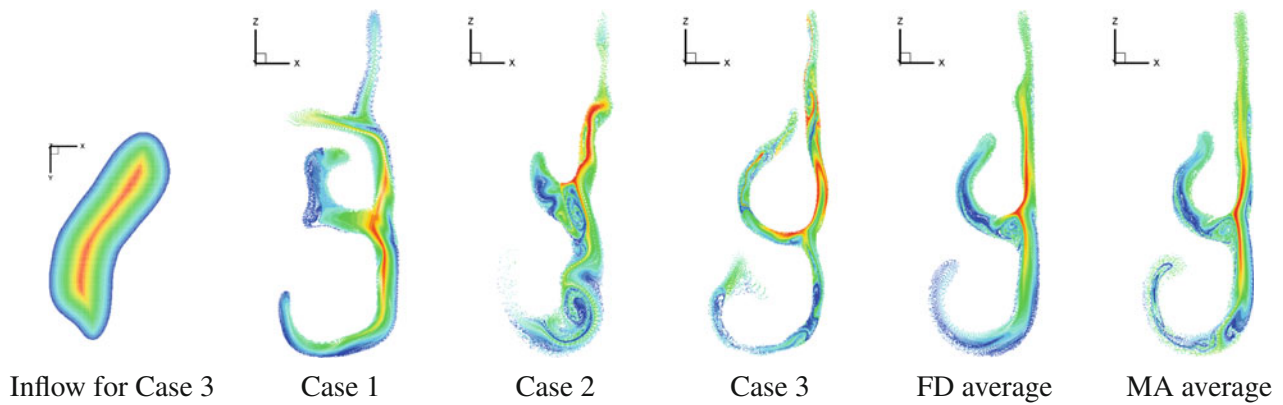
FIGURE 13. Slice of particle tracks colour-coded by distance from the wall at the naris inflow seeding location as shown indicatively for Case 3. The cross-sections correspond to slice MC, as shown in Fig. 1.
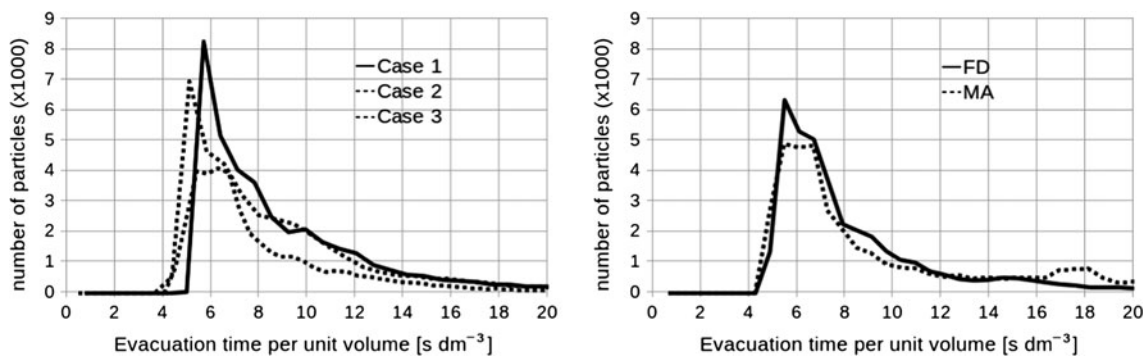

FIGURE 14. Distribution of particle evacuation times, normalized per unit volume of the nasal cavity (see Table 1), for the different cases and average geometries studied.

medial axes approach has a slightly smaller initial peak and a later peak of exiting particles around 0.3 s which is not the case for the other average geometry constructed using FDs. This may be linked to the reduced flow rate in the lower meatus due to the choice of medial axes pruning at the base of the septum in the anterior region of the cavity. However these differences are small in comparison to the similarities and the good representation of the individual cases.

DISCUSSION

There are different approaches to creating a compact representation of the complex geometry of the nasal airways. The two procedures presented here (MA and FDs) have each been shown to be capable of effecting a reversible decomposition of the complex nasal airway geometry, using three healthy subject datasets. Each method relies on initially deconstructing the surface definition into a stack of cross-sections whose location is identified by anatomical landmarks. This ensures correspondence for inter-subject comparison. The cross-sections are then described by use of either FDs or medial axes, where each method has its specific advantages.

The rational and concise description of the nasal cavity by these methods allows for a modal analysis to be formulated. This permits an average (or standard) geometry to be constructed, with subject-specific variations defined by a reduced set of weighted perturbations about the average. The methodology can be extended to different geometric forms.

Both procedures produce coherent, compact representations, leading to similar definitions of average geometries. Differences arise due to the filtering and pruning as based on the underlying description. If neither is performed the individual closed contours are accurately represented. FDs provide a means to reduce model complexity *via* filtering as well as reconstruction *via* modal analysis. The intricate three dimensional airway geometry can be represented as a contour map of modal energy distribution; this offers possibilities for deriving further reductions of the function set or basis required for reconstruction. However a wavelet rather than Fourier representation is likely to be more appropriate as a means to reduce the modes required to represent the entire nasal airway. Further work will

investigate minimal bases for whole nose reconstruction or geometry characterization based on effective energy maps.

On the other hand, the MA method is attractive in providing a convenient method to localise functional regions (e.g., a particular meatus) and the effects of localized variations in inter- and intra-subject geometries. Extensions to the methods have been presented that indicate the versatility and potential for further development of the methods. This includes the use of medial axes in the reconstruction of limited resolution MRI medical images[14] by constructing interpolating medial sheets, altering the medial branch information to simulate localized occlusion or possible surgical interventions, and the use of medial sheets in the delineation of both surface and volume regions of the geometry.

Computational simulations of airflow were performed for steady laminar inspiration for all geometries. In terms of the relation between flow and geometry, these limited results demonstrated that the characteristics of the flow through the averaged geometries were representative of the individual subjects, and largely lay within the range determined for the whole set. However the computations also demonstrated noticeable effects of geometry simplification on some flow parameters. It may be anticipated that for a large sample size, the flow in an averaged geometry may not in fact represent the median of some or all flow measures. The computational effort associated with flow prediction, and the even greater cost of replica model fabrication limits the set of models that can be studied. 'Averaged' geometries are thus attractive as a means to capture flow properties, but these results suggest that care must be taken to ensure the characteristics of the flow are not unduly biased by the inherent regularization associated with averaging. A time-dependent flow study at different phases of the respiratory cycle will enhance the analysis and description of geometrical form in relation to the flow field.

CONCLUSIONS

Two alternative procedures to represent the complex nasal airway geometry have been developed and are compared. Both methods enable different geometries to be averaged while preserving essential anatomic attributes. The averages derived by each method are similar, with both displaying the tendency of averaging to 'iron out' irregularities in the shape of the passageways. Moreover either method provides a technique to quantify geometry and to determine modes of variation about a mean geometric form.

Computations of steady flow were used for a preliminary investigation of the relation between form and patterns of flow in the individual and averaged airway geometries. Each averaged geometry yielded gross flow measures within the range of results obtained from the individual geometries. However in the averaged geometries, the mean wall shear stress and overall pressure drop were below the mean of the corresponding results from the individual models. This is in line with the expected effects of geometry regularization; it indicates potential inadequacies in relying on a standardized anatomical form to represent nasal air flow. Further work is required to apply the methods to a larger range of datasets and to assess the sensitivity of the time-dependent flow to model geometry. Currently the task of reconstruction and the need for user intervention renders the assembly of a large data set difficult. There is nevertheless a steady growth in datasets. Given sufficient data, the methodology described here offers a rational framework for characterising the shape of complex flow conduits, for identifying modes of geometric variation in a population and hence to associate modes of shape variation with consequences for the flow.

APPENDIX

Implicit Function

In brief, the interpolating surface is defined as the zero-level iso-surface of an implicit function $f(\mathbf{x})$. Setting $f(\mathbf{x}) = 0$ on sampled points of the cross-section stack, defines the *on-surface* constraints. A gradient is formed in the implicit function by introducing further constraints at a constant close distance normal to the curve, known as *off-surface* constraints, with $f(\mathbf{x}) < -\lambda$ inside the curves and $f(\mathbf{x}) > \lambda$ outside the curves, where λ is a constant. Interpolation of these constraints leads to the solution of the unknown coefficients $\mathbf{c}$ from a linear system given by $f(\mathbf{x}_i) = \sum_{j=1}^{n} \mathbf{c}_j \phi(\mathbf{x}_i - \mathbf{x}_j)$, for $i = 1, \ldots, n$, where n is the number of constraints. Here the weighting function is given by the cubic RBF (RBF), hence $\phi(\mathbf{x}_i - \mathbf{x}_j) = |\mathbf{x}_i - \mathbf{x}_j|^3$, where $|\cdot|$ denotes the Euclidean norm, $\mathbf{x}_i$ are the position vectors the function is evaluated at and $\mathbf{x}_j$ are the interpolation constraints, for $\mathbf{x}_j = (x_j, y_j, z_j); \quad j = 1, \ldots, n$. This choice of RBF is such that it minimises curvature variation.

The zero-level iso-surface of the implicit function that defines the virtual model surfaces is extracted using the marching tetrahedra approach[5] with linear interpolation to give an initial triangulation, which was then projected onto the true zero-level iso-surface.

To reduce the computational time in the implicit function formulation as well as the marching tetrahedra

method, a partition-of-unity approach[15,37] is used. This divides the global domain of interest into smaller overlapping sub-domains where the problem can be solved locally. The local solutions are combined together by using weighting functions that act as smooth blending functions to obtain the global solution.

Medial Axis

The approach used in this work is the following: a two-dimensional closed curve is defined with edge, E. A medial axis S is then defined as the set of points whose closest distance, D, from the nearest boundary is locally maximum.[22] The local value of D, denoted by d_{ij}, is obtained for a uniform sampling grid centered at the center of mass of E and made up of $n_{\zeta_1} \times n_{\zeta_2}$ points p_{ij}, where $i = 1, \ldots, n_{\zeta_1}, j = 1, \ldots, n_{\zeta_2}, \zeta_1$ and ζ_2 are orthogonal axes of the sampling grid, and ζ_1 is chosen as the major axis of E. The grid is typically formed by choosing $n_{\zeta_1} = 1000$ and maintaining the spacing yields $n_{\zeta_2} \approx 400$ for the middle section of the nasal cavity. If an interrogation point p_{ij} on the grid is inside E then $d_{ij} > 0$ and if outside $d_{ij} < 0$. Hence, a value of $d_{ij} = 0$ signifies that p_{ij} lies on E. If the points on the grid are given an out-of-plane distance proportional to d_{ij}, the object would resemble a hilly landscape where S would be the resultant connected crests (or ridgeline).[11] The local maximum is extracted using a 3×3 local mask and results in a cluster of points that are then connected, ensuring that different branches are identified. Finally interpolation is performed to yield smooth fitting curves that are the medial axes and represent the supporting frame of E.

This procedure is sensitive to the resolution of the evaluation grid, generating spurious or insignificant branches if overly fine. This sensitivity arises if the piecewise linear segments that form E are comparable or larger than the grid scale, and hence at the junction of each segment a MA is formed. High grid sampling is however needed to accurately capture the medial axes. An automatic pruning method is adopted such that each branch is checked to identify spurious terminal branches by calculating its gradient $g = \dfrac{\text{length of branch}}{\text{branch calibre at root}}$. A criterion for the classification of a branch as spurious can be set based on the value of g. In the present case, a limit of $g \leq 1.1$ was found to be robust in determining whether branches should be removed, although the choice is somewhat arbitrary and different values may be required for other datasets. Other pruning methods are described in Weeks et al.,[40] Tam and Heidrich,[35] and Aujay et al.[33] which may be beneficial for other applications. For example an alternative approach is to consider branch lengths, such that if shorter than a given value they can

be considered as small features and removed without significantly altering the object.

The pruning acts as a filter, reducing the level of detail by incrementally removing features of the smallest magnitude. This will therefore also progressively reduce the surface area and volume of the object. A small uniform inflation of the medial axes calibre is hence required, to account for the volume lost due to the pruning procedure. This inflation does not effectively change the surface area of the geometry boundary due to the high aspect ratio of the sections. Details of the surface areas and volumes of the cases studied are detailed in Tables 1 and 2.

Fourier Descriptor

Let us consider a closed curve $\gamma(l)$ that can be expressed as a signal $g(l)$, where l is the perimeter-length at a certain location and $0 \leq l \leq L$, such that the signal has period L. The discrete Fourier expansion of $g(l)$ is formulated by sampling at m equally spaced points to yield $g(k); k = 0, \ldots, m - 1$. The discrete Fourier transform (DFT) is given by

$$c(n) = \frac{1}{m}\sum_{k=0}^{m-1} g(k)e^{-i2\pi nk/m} \quad 0 \leq n \leq m - 1 \quad (1)$$

where $i = \sqrt{-1}$. The real and complex components of $c(n)$ are the FDs, denoted as $R(n)$ and $I(n)$, respectively. The amplitude, or energy, of the nth mode in the series expansion is given by $\sqrt{R(n)^2 + I(n)^2}$. To reconstruct $g(k)$ the inverse discrete Fourier transform (IDFT) is used, which is given by

$$g(k) = \sum_{n=0}^{m-1} c(n)e^{i2\pi nk/m} \quad 0 \leq k \leq m - 1 \quad (2)$$

Signals of the closed curve may be formulated by considering the change in angular direction,[42] however in this work the location in fixed Cartesian coordinate frame[38] is used. The advantage in providing a signal in terms of the angular direction variation along the curve is that only one signal is required, while if using a Cartesian coordinate approach an orthogonal signal for each axis is required. In this work the Cartesian coordinate approach is used since it allows a closed contour to be reconstructed after filtering, averaging or other signal manipulations that is not possible otherwise. A brief description of this approach is now given.

A curve can be described as the change of location coordinates as a function of l, hence implementable directly in $\mathbb{R}^3$ even when the planar cross-sections are not aligned to the Cartesian axes. The signal that describes the curve is given by $g(l) = (x(l) - x(0), y(l) - y(0),$

$z(l) - z(0))$, providing an orthogonal signal for each axis that allows for independent signal modification if desired. It is important to note that since the signals are periodic, a reconstructed closed curve in ensured.

ACKNOWLEDGMENTS

REFERENCES

[1]Anthony, T. R. Contribution of facial feature dimensions and velocity parameters on particle inhalability. *Ann. Occup. Hyg*. 54(6)710–725, 2010.

[2]Aujay, G., F. Hétroy, F. Lazarus, and C. Depraz. Harmonic skeleton for realistic character animation. In: Proceedings of the 2007 ACM SIGGRAPH/Eurographics Symposium on Computer Animation, San Diego, CA, 02–04 August 2007, pp. 151–160.

[3]Baroody, F. M. Functional anatomy of the upper airway in humans. In: *Toxicology of the Nose and Upper Airways*, edited by J. B. Morris and D. J. Shusterman. New York: Informa Healthcare, 2010, pp. 18–44.

[4]Besl, P., and N. McKay. A method for registration of 3-D shapes. *IEEE Trans. Pattern Anal. Mach. Intell*. 14(2):239–256, 1992.

[5]Bloomenthal, J. An implicit surface polygonizer. In: Graphics Gems IV. San Diego: Academic Press Professional, Inc., pp. 324–349, 1994.

[6]Blum, H. A transformation for extracting new descriptors of shape. In: Models for the Perception of Speech and Visual Form. Cambridge: MIT Press, 1967, pp. 362–380.

[7]Carr, J. C., W. R. Fright, and R. K. Beatson. Surface interpolation with radial basis functions for medical imaging. *IEEE Trans. Med. Imaging*. 16(1):96–107, 1997.

[8]Churchill, S. E., L. L. Shacklford, J. N. Georgi, and M. T. Black. Morphological variation and airflow dynamics in the human nose. *Am. J. Hum. Biol*. 16:625–638, 2004.

[9]Doorly, D. J., D. J. Taylor, A. M. Gambaruto, R. C. Schroter, and N. Tolley. Nasal architecture: form and flow. *Philos. Trans. R. Soc. A: Math. Phys. Eng. Sci*. 366(1879): 3225–3246, 2008.

[10]Doorly, D. J., D. J. Taylor, and R. C. Schroter. Mechanics of airflow in the human nasal airways. *Respir. Physiol. Neurobiol*. 163(1–3):100–110, 2008.

[11]D. Eberly, R. Gardner, B. Morse, S. Pizer, and C. Scharlach. Ridges for image analysis. *J. Math. Imaging Vis*. 4(4):353–373, 1994.

[12]Eccles, R. A role for the nasal cycle in respiratory defence. *Eur. Respir. J*. 9(2):371–376, 1996.

[13]Fletcher, P. T., C. Lu, and S. Joshi. Statistics of shape via principal component analysis on lie groups. In: Proceedings of IEEE Computer Society Conference on Computer Vision and Pattern Recognition (CVPR), Vol. 1, pp. 95–101, 2003.

[14]Gambaruto, A. M. Form and Flow in Anatomical Conduits: Bypass Graft and Nasal Cavity. PhD thesis, Aeronautical Engineering, Imperial College, University of London, 2007.

[15]Gambaruto, A. M., D. J. Doorly, and T. Yamaguchi. Wall shear stress and near-wall convective transport: comparisons with vascular remodelling in a peripheral graft anastomosis. *J. Comput. Phys*. 229(14):5339–5356, 2010.

[16]Gambaruto, A. M., A. Moura, and A. Sequeira. Topological flow structures and stir mixing for steady flow in a peripheral bypass graft with uncertainty. *Int. J. Numer. Methods Biomed. Eng*. 26(7): 926–953, 2010.

[17]Gambaruto, A. M., J. Peiro, D. J. Doorly, and A. G. Radaelli. Reconstruction of shape and its effect on flow in arterial conduits. *Int. J. Numer. Methods Fluids*. 57(5):495–517, 2008.

[18]Gambaruto, A. M., D. J. Taylor, and D. J. Doorly. Modelling nasal airflow using a Fourier descriptor representation of geometry. *Int. J. Numer. Methods Fluids*. 59(11):1259–1283, 2009.

[19]Giordana, S., S. J. Sherwin, J. Peiró, D. J. Doorly, Y. Papaharilaou, C. G. Caro, N. Watkins, N. Cheshire, M. Jackson, C. Bicknall, and V. Zervas. Automated classification of peripheral distal by-pass geometries reconstructed from medical data. *J. Biomech*. 38(1):47–62, 2005.

[20]Illum, L. Nasal drug delivery: possibilities, problems and solutions. *J. Control. Release*. 87:187–198, 2003.

[21]Kappagantu, R. V., and B. F. Feenny. Part I: Dynamical Characterization of a Frictionally Excited Beam. *Nonlinear Dyn*. 22(4):317–333, 2000.

[22]Kimmel, R., D. Shaked, and N. Kiryati. Skeletonization via distance maps and level sets. *Comput. Vis. Mach. Underst*. 62(3):382–391, 1995.

[23]Kleven, M., M. C. Melaaen, M. Reimers, J. S. Rotnes, L. Aurdal, and P. G. Djupesland. Using computational fluid dynamics (CFD) to improve the bi-directional nasal drug delivery concept. *Food Bioprod. Process*. 83(C2):107–117, 2005.

[24]Lang, J. Clinical Anatomy of the Nose, Nasal Cavity, and Paranasal Sinuses. New York: Thieme-Stratton Corp., 1989.

[25]Liu, Y., M. R. Johnson, E. A. Matida, S. Kherani, and J. Marsan. Creation of a standardized geometry of the human nasal cavity. *J. Appl. Physiol*. 106(3):784–795, 2009.

[26]Millán, R. D., L. Dempere-Marco, J. M. Pozo, J. R. Cebral, and A. F. Frangi. Morphological characterization of intracranial aneurysms using 3-D moment invariants. *IEEE Trans. Med. Imaging*. 26(9):1270–1282, 2007.

[27]Mygind, N., and D. R. Anatomy. Physiology and function of the nasal cavities in health and disease. *Adv. Drug Deliv. Rev*. 29:3–11, 1998.

[28]Piccinelli, M., A. Veneziani, D. A. Steinman, A. Remuzzi, and L. Antiga. A framework for geometric analysis of vascular structures: application to cerebral aneurysms. *IEEE Trans. Med. Imaging*. 28(8):1141–1155, 2009.

[29]Rennie, C. E.., K. A. Gouder, D. J. Taylor, N. S. Tolley, R. C. Schroter, and D. J. Doorly. Nasal inspiratory flow: at rest and sniffing. *Int. Forum Allergy Rhinol*. 1(2):128–135, 2011.

[30]Rusinkiewicz, S., and M. Levoy. Efficient variants of the ICP Algorithm. In: Proceedings of Third international Conference on 3D Digital Imaging and Modeling (3DIM), Quebec City, Canada, 28 May–1 June 2001.

[31]Schreck, S., K. J. Sullivan, C. M. Ho, and H. K. Chang. Correlations between flow resistance and geometry in a

model of the human nose. *J. Appl. Physiol.* 75(4):1767–1775, 1993.

[32]Schroeter, J. D., J. S. Kimbell, and B. Asgharian. Analysis of particle deposition in the turbinate and olfactory regions using a human nasal computational fluid dynamic model. *J. Aerosol Med.* 19:301–313, 2006.

[33]Shaked, D., and A. M. Bruckstein. Pruning medial axes. *Comput. Vis. Image Underst.* 69(2):156–169, 1998.

[34]Shen, L., J. Ford, F. Makedon, and A. Saykin. A surface-based approach for classification of 3D neuroanatomic structures. *Intell. Data Anal.* 8(6/2004):519–542, 2004.

[35]Tam, R., and W. Heidrich. Shape Simplification Based on the Medial Axis Transform. In: 14th IEEE Visualization 2003 (VIS 2003), Seattle, Washington, 22–24 October 2003.

[36]Taylor, D. J., D. J. Doorly, and R. C. Schroter. Inflow boundary profile prescription for numerical simulation of nasal airflow. *J. R. Soc. Interface.* 7(44):515–527, 2010.

[37]Tobor, I., P. Reuter, and C. Schlick. Efficient Reconstruction of Large Scattered Geometric Datasets using the Partition of Unity and Radial Basis Functions. In: Research Report RR-1301-03, Laboratoire Bordelais de Recherche en Informatique, Université Bordeaux, 2003.

[38]Wang, S., and M. K. Chung. Parametrization and classification of closed anatomical curves. In: Technical Report, 1113, Department of Statistics, University of Wisconsin, 2005.

[39]Wang, Y., X. Gu, P. M. Thompson, and S. Yau. 3D Harmonic Mapping and Tetrahedral Meshing of Brain Imaging Data. In: Proceedings of Medical Imaging Computing and Computer Assisted Intervention (MICCAI), St. Malo, France, 26–30 September 2004.

[40]Weeks, A. R., Jr. Fundamentals of electronic image processing. *SPIE/IEEE Ser Image Sci. Eng.* 333–359, 452–470, 1996.

[41]Wolf, M., S. Naftali, R. C. Schroter, and D. Elad. Air-conditioning characteristics of the human nose. *J. Laryngol. Otol.* 118:87–92, 2004.

[42]Zahn, C. T., and R. Z. Roskies. Fourier descriptors for plane closed curves. *IEEE Trans. Comput.* c-21(3):269–281, 1972.

[43]Zakaria, H., A. M. Robertson, and C. W. Kerber. A parametric model for studies of flow in arterial bifurcations. *Ann. Biomed. Eng.* 36(9):1515–1530, 2008.